


## Article

# Solution Strengthening and Short-Range Order in Cold-Drawn Pearlitic Steel Wires

Gang Zhao <sup>1</sup>, Jianyu Jiao <sup>2</sup>, Yan Wu <sup>2</sup>, Fengmei Bai <sup>1,2,\*</sup>, Hongwei Zhou <sup>3,\*</sup> , Jun Xue <sup>1</sup>, Yixuan Zhu <sup>1</sup> and Guangwen Zheng <sup>2</sup>

<sup>1</sup> State Key Laboratory of Metal Material for Marine Equipment and Application, Anshan 114009, China

<sup>2</sup> School of Metallurgical Engineering, Anhui University of Technology, Maanshan 243002, China

<sup>3</sup> School of Materials Science and Technology, Anhui University of Technology, Maanshan 243002, China

\* Correspondence: baifengmei@ahut.edu.cn (F.B.); hwzhou@ahut.edu.cn (H.Z.); Tel.: +86-17755537045 (F.B.); +86-13855556903 (H.Z.)

**Abstract:** Pearlitic steel rods are subjected to cold-drawing processes to produce pearlitic steel wires with true strains ranging from 0.81 to 2.18. Tensile tests are utilized to attain mechanical properties of cold-drawn pearlitic steel wires. TEM and XRD investigations were performed on the microstructure of the cold-drawn steel wires. With an increasing cold-drawn strain, both the interlamellar spacing and cementite lamellae thickness decrease, while the dislocation density significantly increases. The drawn wire has a tensile strength of 2170 MPa when the true strain reaches 2.18. Deformation-induced cementite dissolution occurs during cold-drawing progress, which releases many C atoms. The findings indicate that the supersaturation of C is heterogeneously distributed in the ferrite matrix. The ordered distribution of the released C in ferrite phases creates short-range order (SRO). SRO clusters and disordered Cottrell atmospheres contribute to solution strengthening, which, together with dislocation strengthening and interlamellar boundary strengthening, form an effective strengthening mechanism in cold-drawn pearlitic steel wires. Our work provides new insights into carbon redistribution and the mechanism of solution strengthening within ferrous phases.

**Keywords:** metals and alloys; pearlitic steel wires; short-range order; solution strengthening; Cottrell atmospheres



**Citation:** Zhao, G.; Jiao, J.; Wu, Y.; Bai, F.; Zhou, H.; Xue, J.; Zhu, Y.; Zheng, G. Solution Strengthening and Short-Range Order in Cold-Drawn Pearlitic Steel Wires. *Crystals* **2024**, *14*, 977. <https://doi.org/10.3390/cryst14110977>

Academic Editor: Dah-Shyang Tsai

Received: 16 October 2024

Revised: 7 November 2024

Accepted: 11 November 2024

Published: 13 November 2024



**Copyright:** © 2024 by the authors. Licensee MDPI, Basel, Switzerland. This article is an open access article distributed under the terms and conditions of the Creative Commons Attribution (CC BY) license (<https://creativecommons.org/licenses/by/4.0/>).

## 1. Introduction

Cold-drawing technology is the main process used to produce high-strength pearlitic steel wires [1,2]. Pearlitic lamellar structures consist of alternating phases of ferrite ( $\alpha$ -Fe) and cementite ( $\theta$ -Fe<sub>3</sub>C). Drawn wires are subject to three distinct strengthening methods, including dislocation strengthening, fine-grain strengthening, and solution strengthening. There are reliable models quantifying both dislocation strengthening and fine-grain strengthening [2–4]. However, the calculated results by several models are distant from the experimental ones [5,6]. It remains challenging to develop an accurate model of solution strengthening due to ongoing controversy about the mechanism of solution strengthening.

The solution strengthening can be attributed to deformation-induced  $\theta$ -Fe<sub>3</sub>C dissolution, which releases C atoms into  $\alpha$ -Fe [7–9]. Several mechanisms have been proposed to explain the  $\theta$ -Fe<sub>3</sub>C dissolution due to plastic deformation: (i) the binding enthalpy between carbon atoms and dislocations in  $\alpha$ -Fe surpassing the solution enthalpy of  $\theta$ -Fe<sub>3</sub>C [10]; (ii) the thinning of  $\theta$ -Fe<sub>3</sub>C lamellae during drawing causing the destabilization of  $\theta$ -Fe<sub>3</sub>C due to an increase in its free energy [11]; (iii) the diffusion of carbon atoms from  $\theta$ -Fe<sub>3</sub>C to the excessive vacancies formed in  $\alpha$ -Fe during cold-drawing [12,13]. Most researchers agree with the solution strengthening from the interaction between dislocations and carbon atoms released from  $\theta$ -Fe<sub>3</sub>C dissolution diffusing into  $\alpha$ -Fe phase. Dislocations are locked down by the so-called carbon Cottrell atmospheres [12,14]. Others propose that a lot of deformation-induced vacancy clusters are believed to play important roles in hardening

the wires, known as defect hardening or strengthening [12,13]. Since vacancies are always associated with carbon, they will not contribute additionally to solid solution hardening [5]. Beside strengthening due to Cottrell atmospheres, solid solution strengthening or hardening originates from the redistribution of carbon [6], which are also obstacles pinning movable dislocations [15].

Carbon solubility in  $\alpha$ -Fe exhibits a positive correlation with cold-drawn strain [16]. This relationship can be revealed through the measurement of thermoelectric power, resistivity, and internal friction [16]. Atom probe tomography (APT) studies have demonstrated the existence of carbon Cottrell atmospheres that are linked to dislocations [14,17]. In the present work, we are not going to propose a new model for solution strengthening. We deeply focus on solution strengthening mechanism. The transmission electron microscope (TEM) analysis reveals the presence of SRO structures in  $\alpha$ -Fe, which is caused by the ordered distribution of carbon. This feature also validates the occurrence of deformation-induced  $\theta$ -Fe<sub>3</sub>C during cold-drawing. Both SRO clusters and Cottrell atmospheres are responsible for solution strengthening. This finding provides new insights into carbon redistribution and the mechanism of solution strengthening within ferrous phases.

## 2. Materials and Methods

The specimen employed in the present investigation is a pearlitic steel wire with the following composition: Fe–0.82C–0.50Mn–0.22Si–0.03Cr in wt.%. The wire rods, initially 7.81 mm in diameter, were patented at 580 °C. The drawing process involved multi-pass drawing with 10 dies. The diameter of the 10 dies decreased continuously. The wire rods underwent cold-drawing processes, resulting in wires with diameters of 5.20 mm, 3.82 mm, and 2.61 mm, at the corresponding true strains ( $\epsilon$ ) of 0.81, 1.43, and 2.18, respectively, where  $\epsilon$  is defined by  $2\ln(d_0/d_i)$  ( $d_0$  is an initial diameter of wire rods and  $d_i$  is a diameter of a cold-drawn wire). The wire rods are presented as  $\epsilon = 0$ .

The tensile testing was measured at room temperature via a universal materials testing machine (CMT 4503, Shenzhen Xinsansi Testing Co., Ltd., Shenzhen, China) at a strain rate of  $3 \times 10^{-3}$ /s. Figure 1a presents the geometry utilized for tensile testing. The length of the wire between the jigs for the tests was 50 times its diameter. For each testing condition, three identical samples were evaluated to determine the mean tensile strength, yielding strength and uniform elongation. The microstructure observations were conducted using a Talos F200X TEM (Thermo Fisher Scientific Inc., Waltham, MA, USA) at an accelerated voltage of 200 kV. For TEM observations, thin foils with a thickness of 40  $\mu$ m were prepared by mechanical polishing and then thinning by ion milling. At the same time, Argon ions were used to remove surface contaminants such as carbon atoms of TEM foils. A Talos F200X TEM was equipped with an Energy Dispersive Spectrometer (EDS) probe with a mapping spatial resolution of 1 nm. X-ray analysis was performed using an Ultima IV diffractometer (Japan Rigaku Corporation, Japan). Before X-ray analysis, the specimens were electrochemically polished to remove deformed zones on the surfaces. The X-ray diffraction (XRD) analysis was performed with Cu K radiation (wavelength,  $\lambda = 0.1542$  nm). The scanning rate of X-ray testing was 0.5°/min, with a step size of 0.02°.

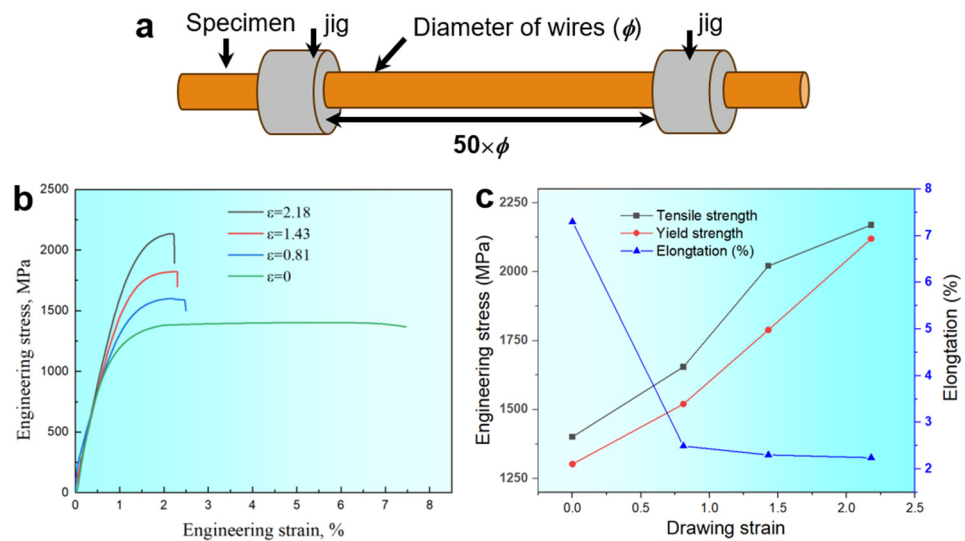


**Figure 1.** (a) Schematic of the tensile specimens; (b) tensile stress–strain curves of wires with the different true stains; (c) tensile strength, yield strength and elongation vs drawn strains.

### 3. Results

#### 3.1. Tensile Properties

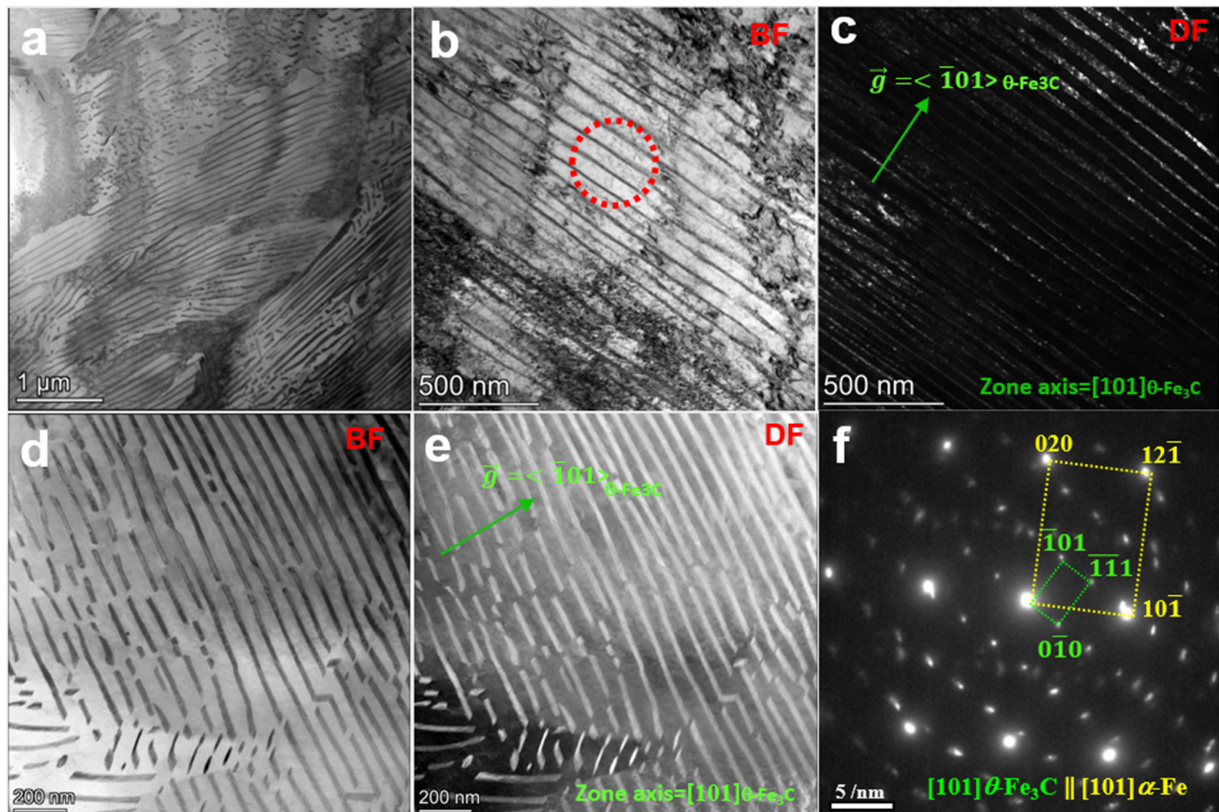
Figure 1b shows the engineering stress–strain curves of the cold-drawn pearlitic wires as a function of  $\epsilon$  ranging from 0 to 2.18. None of the specimens showed a distinct yield point, and hardening was observed up to the ultimate tensile stress. The tensile strength of pearlitic steel rods ( $\epsilon = 0$ ) was found to be about 1401 MPa. With the increase of the drawn strain, the tensile strength, yield strength ( $\sigma_{0.2}$ ) and elongation of the wires gradually increased, as shown in Figure 1c. As the  $\epsilon$  increased to 2.18, the tensile strength was about 2170 MPa.

#### 3.2. TEM Observation

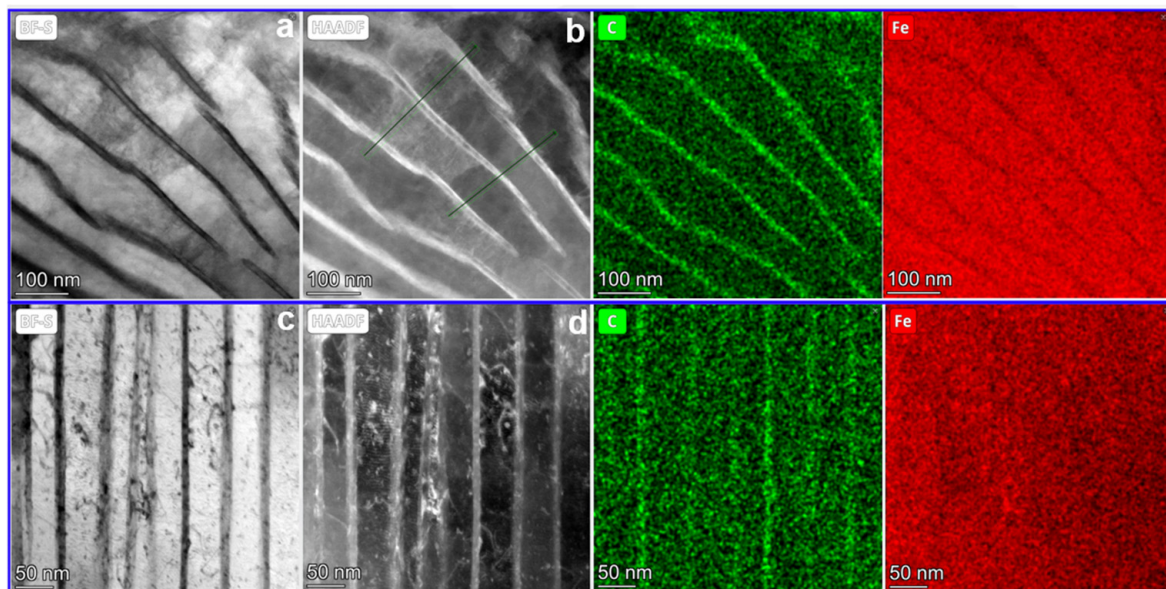
Figure 2 depicts TEM images of wires before cold-drawing. Some lamellae are complete in Figure 2a–c, while some  $\theta\text{-Fe}_3\text{C}$  is broken in Figure 2d,e. Figure 2f displays a selected area electron diffraction pattern (SADP) of lamellar indicated by a circle in Figure 2b. It is deduced from the SADP that two phases have a crystallographic orientation relationship (OR):  $[101]_{\theta\text{-Fe}_3\text{C}} // [101]_{\alpha\text{-Fe}}$  and  $(010)_{\theta\text{-Fe}_3\text{C}} // (111)_{\alpha\text{-Fe}}$ , which is the Isaichev OR, consistent with other reports [8,18]. The orthorhombic crystal structure of  $\theta\text{-Fe}_3\text{C}$  possesses the space group Pbnm, with dimensions  $a = 0.451$  nm,  $b = 0.508$  nm, and  $c = 0.675$  nm [18].

Figure 3 is EDS mapping of pearlitic lamellae at  $\epsilon = 0$  and  $\epsilon = 2.18$ . Before the TEM test, the sample was cleaned by an Argon ion beam to eliminate the influence of surface carbon contamination. At  $\epsilon = 0$ , the lamellae interfaces are clearly visible and the C enrichment in  $\theta\text{-Fe}_3\text{C}$  is significant; at  $\epsilon = 2.18$ , the  $\theta\text{-Fe}_3\text{C}$  lamellae are complete in morphology and the interface is clear, but the C enrichment in  $\theta\text{-Fe}_3\text{C}$  decreases, indicating that under cold-drawing,  $\theta\text{-Fe}_3\text{C}$  is dissolved and the released C atoms diffuse into  $\alpha\text{-Fe}$ .

The TEM images of pearlitic wires with varying  $\epsilon$  are shown in Figure 4. Figure 4(a1,a2) depicts the BF and DF images of  $\alpha\text{-Fe}$  and  $\theta\text{-Fe}_3\text{C}$ , respectively. Figure 4(a4) displays a SADP of the region indicated by a circle in Figure 4(a3). The presence of superlattice  $\{001\}$  spots remarked by arrows in a  $[100]_{\alpha\text{-Fe}}$  zone axis implies that ordered structures are formed in  $\alpha\text{-Fe}$ . Several studies indicate that the ordered carbon configuration in  $\alpha\text{-Fe}$  [19,20] and austenitic steels [21] can lead to SRO formations. In the SRO B2–NiAl phase, the superlattice reflections are also observed at  $\{001\}$  spots in an SADP along the  $[100]_{\alpha\text{-Fe}}$  axis [22]. There are a lot of references about SRO in FCC and BCC alloys/phases validated by additional spots in SADP [22,23]. In Figure 4(a4–c4), the diffraction spots of  $\theta\text{-Fe}_3\text{C}$  with low crystallographic index almost disappear along the  $[100]_{\alpha\text{-Fe}}$  zone axis.



**Figure 2.** TEM images of wires in solution treatment before cold-drawing: (a) pearlitic in different colonies; (b,c) bright field (BF) and dark field (DF) images of complete lamellar; (d,e) BF and DF images of broken  $\theta$ -Fe<sub>3</sub>C; (f) a SADP of lamellar in (b).



**Figure 3.** TEM images and corresponding EDS mapping of wires before and after cold-drawing: (a,b)  $\varepsilon = 0$ ; (c,d)  $\varepsilon = 2.18$ .

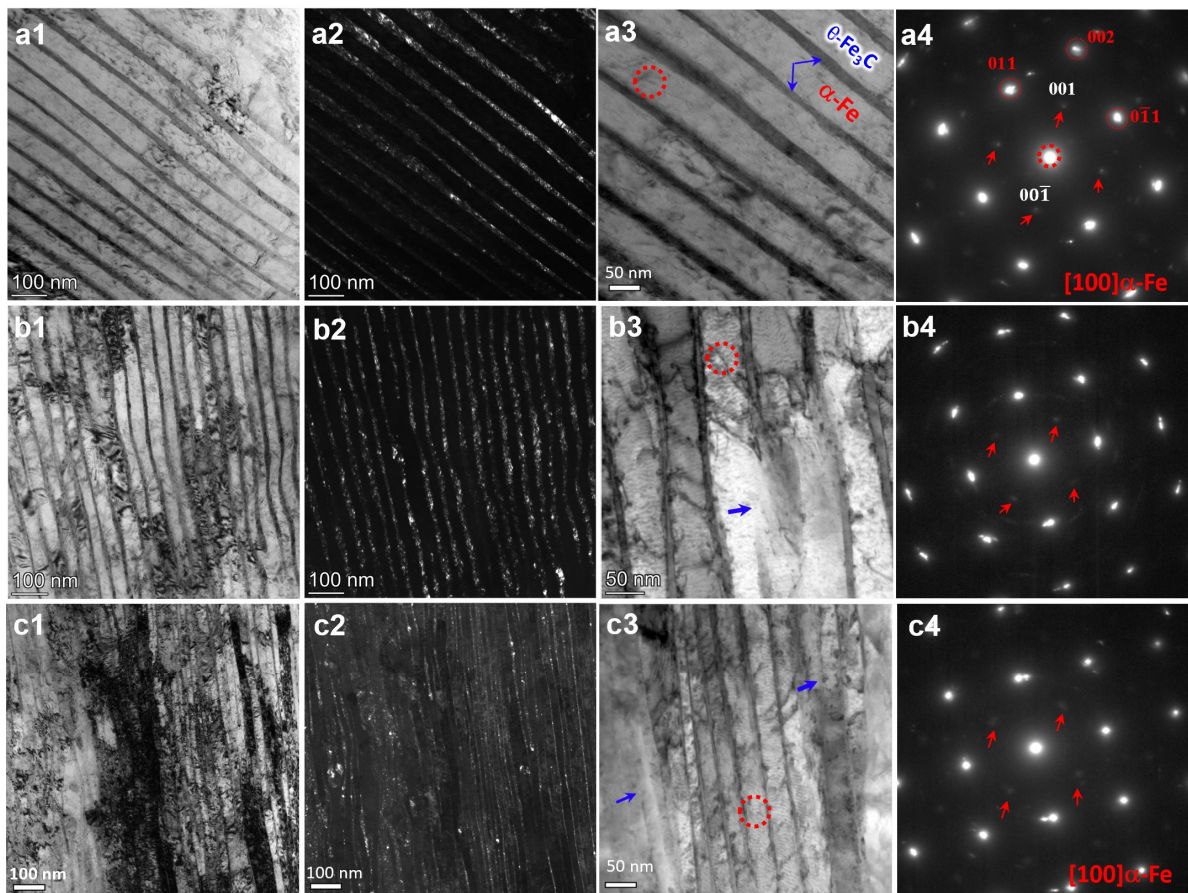


**Figure 4.** TEM images of pearlitic structures: (a) wire rod; (b)  $\varepsilon = 0.81$ ; (c)  $\varepsilon = 2.18$ ; (a1,b1,c1) BF images; (a2,b2,c2) the corresponding DF images; (a3,b3,c3) dislocation configurations in  $\alpha$ -Fe; (a4,b4,c4) SADP of the areas marked by circles in (a3,b3,c3).

At  $\varepsilon = 0.81$ , the lamellae exhibited kinking in Figure 4(b1) and a partial disappearance, as indicated by an arrow in Figure 4(b3). Plastic deformation produces numerous dislocations. The majority of dislocations are distributed throughout  $\alpha$ -Fe lamellae, and the two extremities of the dislocation line are situated in the  $\alpha$ -Fe/ $\theta$ -Fe<sub>3</sub>C boundaries [2]. The dislocation groups in  $\alpha$ -Fe were pinned by the boundaries. Superlattice spots of  $\alpha$ -Fe {001} planes at  $\varepsilon = 0.81$  suggest SRO formations.

Although the strain has reached 2.18, the SRO structure remains stable. The  $\alpha$ -Fe/ $\theta$ -Fe<sub>3</sub>C interface is not clearly visible in Figure 4(c1,c2). As  $\varepsilon$  increases, there is a notable reduction in the length of dislocation lines, accompanied by a corresponding increase in dislocation intensity. Multiple  $\theta$ -Fe<sub>3</sub>C lamellae undergo dissolution, as indicated by the arrows in Figure 4(c3). The dislocation configuration bears resemblance to the structure depicted in Figure 4(b3).

Figure 5 displays interlamellar spacing (ILS) and cementite layers thickness (CLT) as a function of  $\varepsilon$ . This trend is also found in other references [1,9,24]. ILS and CLT can be calculated according to the relationship [25]:

$$r_{\varepsilon} = r_0 \exp(-\varepsilon/2) \quad (1)$$

where  $r_0$  and  $r_{\varepsilon}$  are the original dimensions of lamellar and the ones after cold-drawing with  $\varepsilon$ . Calculated results of ILS and CLT are also illustrated in Figure 5. Measurements of both ILS and CLT are close to the calculated results.

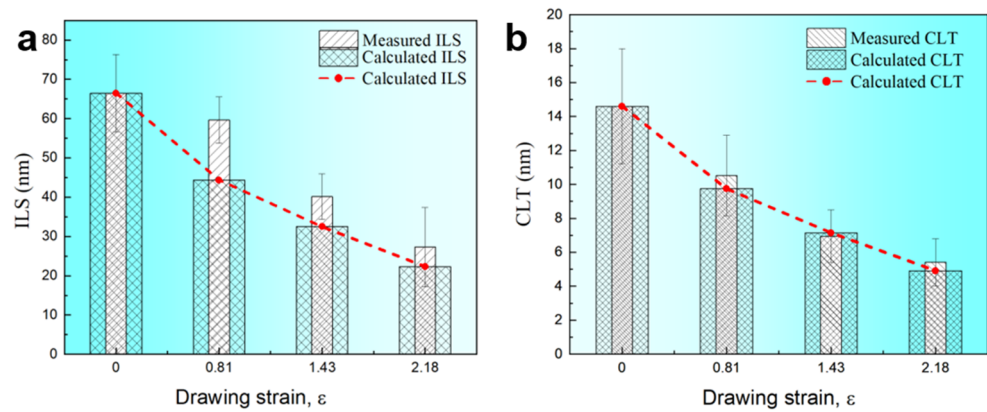


**Figure 5.** Spacing of cold-drawn steel wire lamellae under different strains:(a) interlamellar spacing (ILS); (b) cementite lamellar thickness (CLT).

### 3.3. XRD Analysis

Figure 6 shows XRD patterns of cold-drawn wires with the different  $\epsilon$ . The  $\alpha$ -Fe diffraction peaks of the (110), (200), (211), (220), and (310) planes can be identified according to bcc crystal patterns. But the  $\alpha$ -Fe diffraction peaks show broadening, which is resulting from a refinement of pearlitic lamellae and an increase in dislocation density during the cold-drawing process [26]. At  $\epsilon = 0$ , diffraction peaks from  $\theta$ -Fe<sub>3</sub>C can be observed, while these peaks almost disappear with the increase of  $\epsilon$ . Deformation-induced  $\theta$ -Fe<sub>3</sub>C dissolution and  $\theta$ -Fe<sub>3</sub>C amorphization may be responsible for the disappearance of  $\theta$ -Fe<sub>3</sub>C diffraction peaks [7,26].

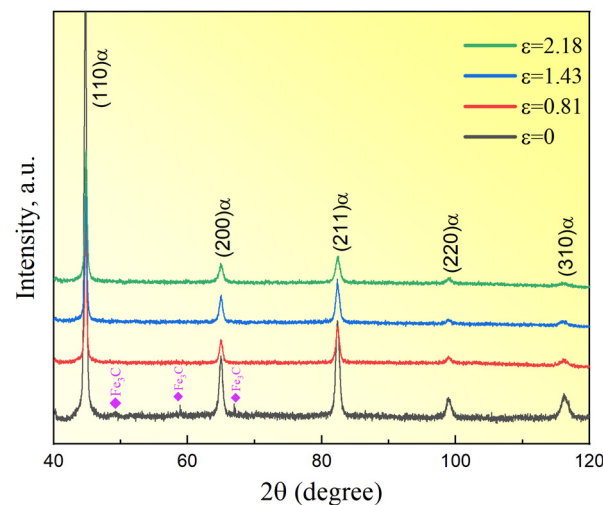


**Figure 6.** XRD patterns of cold-drawn wires.

Generally, the XRD peak widening is related to dislocation density, which can be determined using the following Williamson–Hall equations [27]:

$$\beta \frac{\cos\theta_{hkl}}{\lambda} = \frac{1}{D} + 2e \frac{\sin\theta_{hkl}}{\lambda} \quad (2)$$

where  $\beta$ ,  $\theta_{hkl}$ ,  $\lambda$ ,  $e$  and  $D$ , are the half-height width of the diffraction peaks (hkl), the diffraction angle at the selected peak position, X-ray wavelength (0.1542 nm), the effective mean microstrain, and the average grain size, respectively. In Formula (2), the broadening of the diffraction peak caused by the grain size becomes significantly pronounced only when the grain size is less than 100 nm. In Figure 2a, the size of the pearlitic clusters/grains is several micrometers, indicating that  $1/D$  is relatively small and can be ignored here. Therefore, the linear fitting diagram of  $\beta \frac{\cos\theta_{hkl}}{\lambda}$  and  $\frac{\sin\theta_{hkl}}{\lambda}$  for different  $\alpha$ -Fe diffraction

peaks of (110), (200), (211), and (220) can generate the slope of  $2e$ . The linear fitting plots for the wires with the different  $\varepsilon$  are shown in Figure 7a.

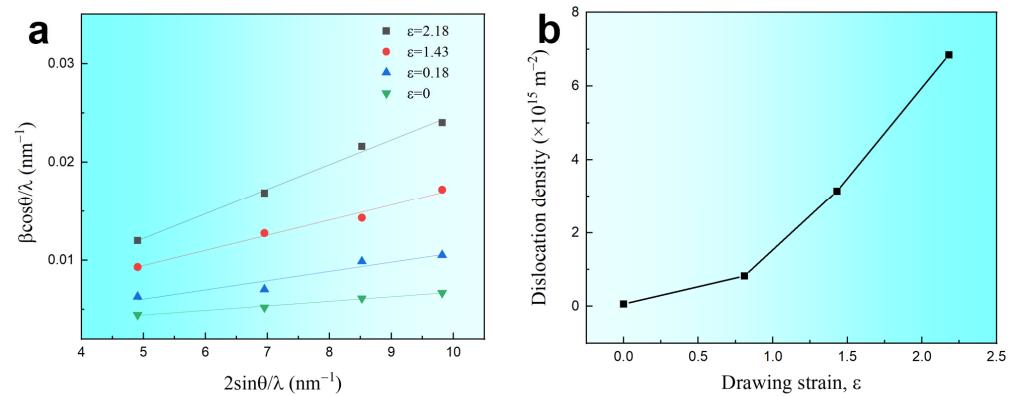


**Figure 7.** The dislocation density ( $\rho$ ) of the cold-drawn wires: (a) linear fitting plots for the diffraction patterns of the wires in Figure 6; (b)  $\rho$  as the function of  $\varepsilon$ .

The dislocation density,  $\rho$ , is then calculated using the following Equation [3]:

$$\rho = 14.4 \frac{e^2}{b^2} \quad (3)$$

where  $\rho$ ,  $e$  and  $b$  are the dislocation density, the effective mean microstrain, and the Burgers vector (0.246 nm), respectively. Substituting  $e$  into Equation (3) to obtain  $\rho$ , Figure 7b illustrates the dislocation density increase with  $\varepsilon$ . At  $\varepsilon = 0.81$ , the dislocation density slowly increases, while it significantly increases when  $\varepsilon$  rises from 0.81 to 2.18. Dislocation densities at  $\varepsilon = 0$  and  $\varepsilon = 2.18$  are  $6.2 \times 10^{14}$  and  $6.8 \times 10^{15} \text{ m}^{-2}$ , respectively, which are in the same order of magnitude as the values measured by XRD [13], TEM [2], and transmission Kikuchi diffraction (TKD) methods [4].

## 4. Discussion

### 4.1. Strengthening Mechanism

There are three strengthening mechanisms in cold-drawn pearlitic steel wires: (i) boundary strengthening ( $\sigma_b$ ), (ii) dislocation strengthening ( $\sigma_\rho$ ), and (iii) solution strengthening ( $\sigma_{ss}$ ). The flow stress or yield stress ( $\sigma_{0.2}$ ) of cold-drawn pearlitic wires during tensile is described by [2]:

$$\sigma_{0.2} = \sigma_0 + \sigma_b + \sigma_\rho + \sigma_{ss} \quad (4)$$

Boundary strengthening results from nanoscale  $\theta$ -Fe<sub>3</sub>C lamellae, which act as obstacles to dislocation glide between  $\alpha$ -Fe lamellae. It can be estimated via the Hall–Petch relationship, as follows [2]:

$$\sigma_b = \sigma_0 + k(d)^{-0.5} \quad (5)$$

where  $\sigma_0$  is the friction stress of pure  $\alpha$ -Fe, and  $\sigma_0$  is taken as 60 MPa.  $k$  is the slope of the Hall–Petch equation, and  $k = 0.31 \text{ MPamm}^{-0.5}$  in the present work, which is reported from measurements over a wide strain range [28].  $d$  is the width of the  $\alpha$ -Fe lamellae, as shown in Figure 5.

Dislocation strengthening is associated with the interactions of dislocations. The increase in flow stress is given by [5,28]:

$$\sigma_\rho = \alpha M G b \rho^{0.5} \quad (6)$$

where  $\alpha$  is a constant of 0.24;  $M$  is the orientation factor, about 1.84 for the strong  $\langle 110 \rangle$  of Fe [28];  $G$  is the shear modulus (77.5 GPa [2]);  $b$  is the Burgers vector, 0.248 nm for  $\alpha$ -Fe; and  $\rho$  is the dislocation density, which is based on XRD patterns, as show in Figure 7b. The calculated  $\sigma_b$

and  $\sigma_\rho$  based on Equations (5) and (6), respectively, together with the measurements of yield stress are shown in Figure 8. Both  $\sigma_b$  and  $\sigma_\rho$  increase with  $\varepsilon$ .  $\sigma_b$  is much higher than  $\sigma_\rho$  at all strains, which means that boundary strengthening is prominent in cold-drawn pearlitic steel wires. This feature is consistent with other results [25]. The combination of  $\sigma_b$  and  $\sigma_\rho$  is a little lower than experimental results at different  $\varepsilon$ . This trend indicates that there is a solution strengthening mechanism beside boundary strengthening and dislocation strengthening in the cold-drawn pearlitic steel wires.

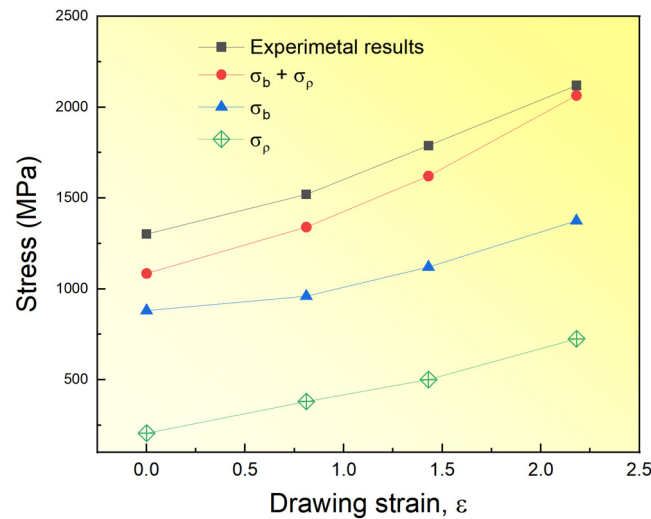


**Figure 8.** The calculated and experimental strengthening of cold-drawn pearlitic steel wires.

#### 4.2. Cottrell Atmosphere Strengthening

Figure 7b based on XRD patterns reveals the dislocation density of the entire steel wire, while the distribution of dislocation density in  $\alpha$ -Fe and  $\theta$ -Fe<sub>3</sub>C phase remains ambiguous. Geometric phase analysis (GPA) is a method for mapping the strain field from high-resolution TEM (HRTEM) micrographs. The strain mapping calculated by the GPA method is related to the lattice dislocations, which can directly show the dislocation density distribution [29].

Figure 9 displays HRTEM images of  $\alpha$ -Fe/ $\theta$ -Fe<sub>3</sub>C lamellae. Prior to drawing,  $\theta$ -Fe<sub>3</sub>C displays a platelet-like morphology in the wires, as depicted in Figure 9(a1). Fast Fourier Transform (FFT) patterns imply that both phases exhibit single crystalline at  $\varepsilon = 0$ . The HRTEM image in Figure 9(a3), obtained by magnifying the yellow square in Figure 9(a1), demonstrates an Isaichev OR between  $\alpha$ -Fe and  $\theta$ -Fe<sub>3</sub>C phases. Figure 9(b1) displays bending  $\theta$ -Fe<sub>3</sub>C lamellae at  $\varepsilon = 2.18$ , with blurred interphase boundaries. The thickness of  $\theta$ -Fe<sub>3</sub>C lamellae in Figure 9(b1) decreases as  $\varepsilon$  increases. The FFT patterns of the  $\alpha$ -Fe phase and  $\theta$ -Fe<sub>3</sub>C in Figure 9(b2) are similar to those in Figure 9(a2).

The strain mapping using GPA method is shown in Figure 9(a4,b4) and only the strain component  $\varepsilon_{xx}$  is depicted. Prior to drawing, strain concentrations are mostly observed at the  $\alpha$ -Fe/ $\theta$ -Fe<sub>3</sub>C interface in Figure 9(a4). Additionally, the strain is uniformly distributed throughout  $\alpha$ -Fe. This observation suggests that the dislocation densities are low prior to the cold-drawing process. When  $\varepsilon$  reaches 2.18, there are noticeable strain concentrations within  $\alpha$ -Fe and at the interphase boundaries, as shown in Figure 9(b4). The dislocation densities rapidly increase due to plastic deformation of both phases caused by cold-drawing, as shown in Figure 7b. The distribution of strain inside the  $\alpha$ -Fe phase exhibits non-uniformity, with certain regions experiencing higher levels of strain compared to others.

Significant strain concentrations suggests that a large number of dislocations are formed in the regions surrounding the interphase boundaries during cold-drawing at  $\varepsilon = 2.81$ , in comparison to that before drawing. The diffusion of C atoms in a solid solution into the dislocation cores is facilitated by the strong interaction between C and dislocations [10]. Dislocations are locked down by so-called Cottrell atmospheres, as



described in reference [12,14]. Cottrell atmospheres segregated into dislocations have been proven by APT studies [14,17]. Disordered Cottrell atmospheres are considered in the solution strengthening contributions in cold-drawn pearlitic steel wires. In martensitic steels [20] and low carbon steels [30], Cottrell atmosphere strengthening is also investigated.

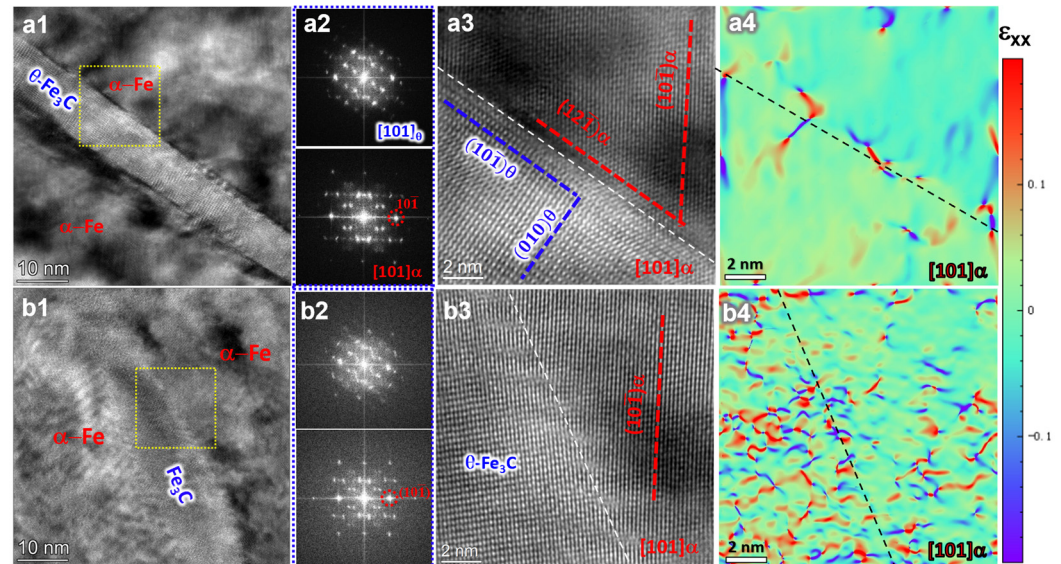


**Figure 9.** HRTEM images of  $\alpha$ -Fe/ $\theta$ -Fe<sub>3</sub>C interfaces at: (a)  $\varepsilon = 0$ , (b)  $\varepsilon = 2.18$ . (a2,b2) The FFT patterns of  $\alpha$ -Fe and  $\theta$ -Fe<sub>3</sub>C phases in (a1,b1), respectively; (a3,b3) magnified view of the yellow box areas in (a1,b1); and (a4,b4) the corresponding strain maps along the  $[100]_{\alpha\text{-Fe}}$  axis calculated by Strain++ software V1.8 for HRTEM images in (a3,b3).

#### 4.3. SRO Cluster Strengthening

Solution-treated steel wires have low dislocation density, as shown in Figures 7b and 9(a4), as well as very low vacancy concentration. At the same time, carbon concentration is much lower in  $\alpha$ -Fe than in  $\theta$ -Fe<sub>3</sub>C, which is also verified by APT [6]. Therefore, Cottrell atmosphere strengthening is weaker than that in cold-drawn conditions. SRO clusters are observed in cold-drawn pearlitic steel wires before and after the different strains. It is generally believed that the formation of SRO is related to interstitial atoms, such as C, boron (N), nitrogen (N), and hydrogen (H) [31,32]. Kim et al. [23] report the influence of C addition on the mechanical properties of high-Mn TRIP steels and find that C can be used to manipulate plastic instability and SRO clusters. In Fe-40Ni-15Cr-0.25 N (wt.%) austenitic stainless steel, Grujicic et al. [33] determined that N strongly tends to occupy interstitial sites with high concentrations of Cr atoms, which results in the formation of SRO clusters. In B-doped high-entropy alloys (HEA), it is found that soluble B increases the stress/strain field at the recrystallized HEA grain structure, leading to the generation of SRO in those deformation structures under loading [34]. Lu et al. [35] also find that SRO is a result of ordered interstitial complexes in the BCC HEAs doped with either 2.0 at % O or N, (Ta<sub>0.5</sub>Nb<sub>0.5</sub>HfZrTi)<sub>98</sub>O<sub>2</sub> and (Ta<sub>0.5</sub>Nb<sub>0.5</sub>HfZrTi)<sub>98</sub>N<sub>2</sub>.

The octahedral position pertaining to C interstitial atoms can result in SRO in the pearlitic steels and other BCC alloys. There may be other C configurations or clusters that are responsible for SRO. Numerous studies suggest that the formation of SRO in high-Mn steel originates from Mn-C clusters [36]. Kim et al. [23] suggest that an SRO structure is caused by the short-range clustering (SRC) of carbon vacancies (CV), which is referred to as CV SRO. CV pairs can be more easily formed by a short-range C ordering than Mn-C clusters. In austenitic steels, the mechanism of interstitial-interstitial (i-i) atom pair re-orientation is responsible for SRO, rather than re-orientation of interstitial-substitutional (i-s) atoms and interstitial atom-vacancy (i-v) pairs re-orientation [37]. In our work, there are few accounts of substitutional Mn and Cr elements in the pearlitic steel

with the composition of Fe–0.82C–0.50Mn–0.22Si–0.03Cr in wt.%, and C is the dominant interstitial atom. Consequently, i–s pairs are not the factor for SRO. Dislocation density and vacancies are much lower in solution-treated conditions. Therefore, the C ordered arrangement results in SRO clusters. Deformation-induced vacancies are easily formed in cold-drawn conditions, meaning that SRO could be related with CV-ordered clusters in the pearlitic steels.

The dislocation density increases with  $\epsilon$ , as presented in Figure 7b. If only the carbon atoms in  $\alpha$ -Fe phases diffuse into dislocations to form disordered Cottrell atmospheres, the initial SRO structure will be quickly broken down by cold-drawing. Nevertheless, SRO constructions continue to maintain their prevalence at  $\epsilon = 2.18$ . This finding suggests that there exists a sufficient quantity of carbon resources that can diffuse into both the ordered sites and dislocation cores. Only deformation-induced  $\theta$ -Fe<sub>3</sub>C dissolution can yield a large number of C atoms. The dislocations are predominantly distributed within the  $\alpha$ -Fe lamellae, as depicted in Figure 9(a3–c3). The interphase borders pin both ends of the dislocation lines during the cold-drawing, causing the accumulation of dislocations along the boundaries (Figure 9(b4)). Based on the results of EDS mapping in Figure 3, XRD patterns in Figure 6, GPA analysis in Figure 9, and other findings [8], the strong interaction between dislocations and  $\theta$ -Fe<sub>3</sub>C leads to the dissolution and amorphization of  $\theta$ -Fe<sub>3</sub>C. A robust carbon-dislocation interaction in  $\alpha$ -Fe enhances the solution of carbon atoms in  $\alpha$ -Fe [16,38]. It is advantageous for the production of both SRO clusters and disordered Cottrell atmospheres when carbon is present in a solid solution in  $\alpha$ -Fe phase. SRO clusters in the present study further verify the transfer of carbon atoms from dissolved  $\theta$ -Fe<sub>3</sub>C to the  $\alpha$ -Fe phase, as well as the carbon supersaturation of the  $\alpha$ -Fe phase in the cold-drawn wires.

Dislocation density is much higher in cold-drawn conditions than in solution treatment while the dislocation density distribution is locally non-uniform, as shown in Figure 9(b4). The disordered Cottrell atmospheres and SRO clusters are both generated in cold-drawn pearlitic steel wires. This feature indicates that the C amount corresponding to a high supersaturation is heterogeneously distributed in the  $\alpha$ -Fe matrix.

The strengthening of SRO clusters has been proved in HEAs [35,39,40], low-carbon steel [30], and austenitic stainless steels [31,41,42]. It can be concluded that this strengthening mechanism also plays a role in drawn steel wires. Consequently, solution strengthening in the present work can be ascribed to both disordered Cottrell atmospheres and SRO clusters. This finding may be useful for proposing a new model of solution strengthening.

## 5. Conclusions

- (1) With increasing cold-drawn strains, both the interlamellar spacing and cementite lamellae thickness decrease, while dislocation densities significantly increase. The drawn wire has a tensile strength of 2170 MPa when the true strain reaches 2.18. Both disordered Cottrell atmospheres and SRO clusters are formed in cold-drawn pearlitic steel wires. SRO clusters and disordered Cottrell atmospheres contribute to solution strengthening which, together with dislocation strengthening and interlamellar boundary strengthening, form an effective strengthening mechanism in cold-drawn pearlitic steel wires.
- (2) Deformation-induced cementite dissolution occurs during cold-drawing progress, which releases many C atoms. Both the supersaturation of C and the dislocation density are heterogeneously distributed in the  $\alpha$ -Fe matrix. The strong binding between C atoms and dislocation leads to the creation of disordered Cottrell atmospheres.
- (3) SRO clusters are formed both before and after the heavy cold-drawing in pearlitic steel wires. The ordered distribution of the released C from cementite dissolution within ferrite phases creates short-range order (SRO). SRO clusters are formed both before and after the heavy cold-drawing in pearlitic steel wires, which validates the occurrence of deformation-induced  $\theta$ -Fe<sub>3</sub>C dissolution. The ordered distribution of C released by  $\theta$ -Fe<sub>3</sub>C dissolution in  $\alpha$ -Fe phases generates SRO clusters.

**Author Contributions:** Conceptualization, G.Z. (Gang Zhao), J.J., F.B. and H.Z.; methodology, G.Z. (Gang Zhao), J.J., F.B. and H.Z.; validation, G.Z. (Gang Zhao), J.J., Y.W. and H.Z.; formal analysis, G.Z. (Gang Zhao), J.J., Y.W., J.X. and Y.Z.; investigation, G.Z. (Gang Zhao), J.J., F.B., H.Z., J.X. and Y.Z.; data curation, G.Z. (Gang Zhao), J.J., Y.W., F.B., H.Z., J.X. and Y.Z.; writing—original draft preparation, G.Z. (Gang Zhao), F.B. and H.Z.; writing—review and editing, G.Z. (Gang Zhao), F.B., H.Z. and G.Z. (Guangwen Zheng); project administration, F.B., H.Z. and G.Z. (Guangwen Zheng); funding acquisition, F.B. and H.Z. All authors have read and agreed to the published version of the manuscript.

**Funding:** This research was funded by Natural Science Foundation of China, grant number 52174359, and Natural Science Foundation of Anhui, grant numbers 2022AH050325 and 2022AH050327, Domestic Visit and Training Project of Young Backbone Teachers in Anhui Province, grant number JNFX2024012, and Overseas Visit and Training Project of Young Backbone Teachers in Anhui Province, grant number JWFX2023012.

**Data Availability Statement:** The original contributions presented in the study are included in this article, further inquiries can be made available by the corresponding author.

**Conflicts of Interest:** The authors declare no conflicts of interest.

## References

- Wei, D.; Wang, L.; Hu, X.; Fang, F. Fabricating iron wires with superior strength–ductility combination through a gradient lamellar structure. *Mater. Lett.* **2021**, *304*, 130644. [[CrossRef](#)]
- Zhang, X.; Godfrey, A.; Huang, X.; Hansen, N.; Liu, Q. Microstructure and strengthening mechanisms in cold-drawn pearlitic steel wire. *Acta Mater.* **2011**, *59*, 3422–3430. [[CrossRef](#)]
- Takebayashi, S.; Kunieda, T.; Yoshinaga, N.; Ushioda, K.; Ogata, S. Comparison of the Dislocation Density in Martensitic Steels Evaluated by Some X-ray Diffraction Methods. *ISIJ Int.* **2010**, *50*, 875–882. [[CrossRef](#)]
- Li, Y.; Goto, S.; Kostka, A.; Herbig, M. Local measurement of geometrically necessary dislocation densities and their strengthening effect in ultra-high deformed pearlite. *Mater. Charact.* **2023**, *203*, 113132. [[CrossRef](#)]
- Borchers, C.; Kirchheim, R. Cold-drawn pearlitic steel wires. *Prog. Mater. Sci.* **2016**, *82*, 405–444. [[CrossRef](#)]
- Borchers, C.; Al-Kassab, T.; Goto, S.; Kirchheim, R. Partially amorphous nanocomposite obtained from heavily deformed pearlitic steel. *Mater. Sci. Eng. A* **2009**, *502*, 131–138. [[CrossRef](#)]
- Guelton, N.; François, M. Strain-Induced Dissolution of Cementite in Cold-Drawn Pearlitic Steel Wires. *Metall. Mater. Trans. A* **2020**, *51*, 1602–1613. [[CrossRef](#)]
- Zhou, Y.T.; Shao, X.H.; Zheng, S.J.; Ma, X.L. Structure evolution of the Fe<sub>3</sub>C/Fe interface mediated by cementite decomposition in cold-deformed pearlitic steel wires. *J. Mater. Sci. Technol.* **2022**, *101*, 28–36. [[CrossRef](#)]
- Yang, X.; Bao, S.; Kang, X.; Hu, J.; Liu, C.; Tian, R. Evolution of Microstructure and Fe/Fe<sub>3</sub>C Interface Structure in Cold-Drawn Pearlitic Steel Wires. *Steel Res. Int.* **2024**, *95*, 2300556. [[CrossRef](#)]
- Gavriljuk, V.G. Decomposition of cementite in pearlitic steel due to plastic deformation. *Mater. Sci. Eng. A* **2003**, *345*, 81–89. [[CrossRef](#)]
- Languillaume, J.; Kapelski, G.; Baudelet, B. Cementite dissolution in heavily cold drawn pearlitic steel wires. *Acta Mater.* **1997**, *45*, 1201–1212. [[CrossRef](#)]
- Takahashi, J.; Kosaka, M.; Kawakami, K.; Tarui, T. Change in carbon state by low-temperature aging in heavily drawn pearlitic steel wires. *Acta Mater.* **2012**, *60*, 387–395. [[CrossRef](#)]
- Chen, Y.Z.; Csiszár, G.; Cizek, J.; Westerkamp, S.; Borchers, C.; Ungár, T.; Goto, S.; Liu, F.; Kirchheim, R. Defects in Carbon-Rich Ferrite of Cold-Drawn Pearlitic Steel Wires. *Metall. Mater. Trans. A* **2013**, *44*, 3882–3889. [[CrossRef](#)]
- Hutchinson, B.; Hagström, J.; Karlsson, O.; Lindell, D.; Tornberg, M.; Lindberg, F.; Thuvander, M. Microstructures and hardness of as-quenched martensites (0.1–0.5% C). *Acta Mater.* **2011**, *59*, 5845–5858. [[CrossRef](#)]
- Cottrell, A.H.; Bilby, B.A. Dislocation Theory of Yielding and Strain Ageing of Iron. *Proc. Phys. Soc. A* **1949**, *62*, 49. [[CrossRef](#)]
- Lamontagne, A.; Massardier, V.; Kléber, X.; Sauvage, X.; Mari, D. Comparative study and quantification of cementite decomposition in heavily drawn pearlitic steel wires. *Mater. Sci. Eng. A* **2015**, *644*, 105–113. [[CrossRef](#)]
- Min, N.; Li, W.; Li, H.; Jin, X. Atom Probe and Mössbauer Spectroscopy Investigations of Cementite Dissolution in a Cold Drawn Eutectoid Steel. *J. Mater. Sci. Technol.* **2010**, *26*, 776–782. [[CrossRef](#)]
- Bhadeshia, H.K.D.H. Cementite. *Int. Mater. Rev.* **2020**, *65*, 1–27. [[CrossRef](#)]
- Zhang, X.; Wang, H.; Hickel, T.; Rogal, J.; Li, Y.; Neugebauer, J. Mechanism of collective interstitial ordering in Fe–C alloys. *Nat. Mater.* **2020**, *19*, 849–854. [[CrossRef](#)]
- Zhou, H.W.; Fang, J.F.; Chen, Y.; Yang, L.; Zhang, H.; Lu, Y.; He, Y.Z. Internal friction studies on dynamic strain aging in P91 ferritic steel. *Mater. Sci. Eng. A* **2016**, *676*, 361–365. [[CrossRef](#)]
- Pham, M.S.; Holdsworth, S.R. Dynamic strain ageing of AISI 316L during cyclic loading at 300 °C: Mechanism, evolution, and its effects. *Mater. Sci. Eng. A* **2012**, *556*, 122–133. [[CrossRef](#)]

22. Zhou, B.C.; Yang, T.; Zhou, G.; Wang, H.; Luan, J.H.; Jiao, Z.B. Mechanisms for suppressing discontinuous precipitation and improving mechanical properties of NiAl-strengthened steels through nanoscale Cu partitioning. *Acta Mater.* **2020**, *205*, 116561. [[CrossRef](#)]
23. Seol, J.B.; Kim, J.; Na, S.H.; Park, C.G.; Kim, H.S. Deformation rate controls atomic-scale dynamic strain aging and phase transformation in high Mn TRIP steels. *Acta Mater.* **2017**, *131*, 187–196. [[CrossRef](#)]
24. Toribio, J.; Ayaso, F.-J.; Rodríguez, R. Pearlite Interlamellar Spacing and Vickers Micro-Hardness in the Necking Region of Cold-Drawn Pearlitic Steel Wires. *Metals* **2023**, *13*, 1401. [[CrossRef](#)]
25. Zhang, X.; Hansen, N.; Godfrey, A.; Huang, X. Dislocation-based plasticity and strengthening mechanisms in sub-20 nm lamellar structures in pearlitic steel wire. *Acta Mater.* **2016**, *114*, 176–183. [[CrossRef](#)]
26. Wei, D.; Min, X.; Hu, X.; Xie, Z.; Fang, F. Microstructure and mechanical properties of cold drawn pearlitic steel wires: Effects of drawing-induced heating. *Mater. Sci. Eng. A* **2020**, *784*, 139341. [[CrossRef](#)]
27. Williamson, G.K.; Smallman, R.E., III. Dislocation densities in some annealed and cold-worked metals from measurements on the X-ray debye-scherrer spectrum. *Philos. Mag. A J. Theor. Exp. Appl. Phys.* **1956**, *1*, 34–46. [[CrossRef](#)]
28. Feng, H.; Wang, L.; Cui, S.; Hansen, N.; Fang, F.; Zhang, X. Microstructure and strengthening mechanisms of nanolamellar structures in ultrastrong drawn iron wires. *Scripta Mater.* **2021**, *200*, 113906. [[CrossRef](#)]
29. Hÿtch, M.J.; Snoeck, E.; Kilaas, R. Quantitative measurement of displacement and strain fields from HREM micrographs. *Ultramicroscopy* **1998**, *74*, 131–146. [[CrossRef](#)]
30. Yuan, X.; Li, W.; Pang, Q.; Zhang, C.; Lu, G. Study on the performance and strain aging behavior of solid-solution state low-carbon steel. *Mater. Sci. Eng. A* **2018**, *726*, 282–287. [[CrossRef](#)]
31. Chu, K.; Antillon, E.; Stewart, C.; Knipling, K.; Callahan, P.; Wu, S.; Rowenhorst, D.; McDowell, D.L. Investigation of chemical short range order strengthening in a model Fe–12Ni–18Cr (at. %) stainless steel alloy: A modeling and experimental study. *Acta Mater.* **2023**, *261*, 119385. [[CrossRef](#)]
32. Kim, J.-M.; Kim, S.-J.; Kang, J.-H. Effects of short-range ordering and stacking fault energy on tensile behavior of nitrogen-containing austenitic stainless steels. *Mater. Sci. Eng. A* **2022**, *836*, 142730. [[CrossRef](#)]
33. Grujicic, M.; Owen, W.S. Models of short-range order in a face-centered cubic Fe-Ni-Cr alloy with a high concentration of nitrogen. *Acta Metall. Mater.* **1995**, *43*, 4201–4211. [[CrossRef](#)]
34. Seol, J.B.; Bae, J.W.; Kim, J.G.; Sung, H.; Li, Z.; Lee, H.H.; Shim, S.H.; Jang, J.H.; Ko, W.-S.; Hong, S.I.; et al. Short-range order strengthening in boron-doped high-entropy alloys for cryogenic applications. *Acta Mater.* **2020**, *194*, 366–377. [[CrossRef](#)]
35. Lei, Z.; Wu, Y.; He, J.; Liu, X.; Wang, H.; Jiang, S.; Gu, L.; Zhang, Q.; Gault, B.; Raabe, D.; et al. Snoek-type damping performance in strong and ductile high-entropy alloys. *Sci. Adv.* **2020**, *6*, eaba7802. [[CrossRef](#)] [[PubMed](#)]
36. Wesselmecking, S.; Song, W.; Bleck, W. Dynamic and Static Strain Aging in a High-Manganese Steel. *Steel Res. Int.* **2022**, *93*, 2100707. [[CrossRef](#)]
37. Karlsen, W.; Ivanchenko, M.; Ehrnstén, U.; Yagodzhinskyy, Y.; Hänninen, H. Microstructural manifestation of dynamic strain aging in AISI 316 stainless steel. *J. Nucl. Mater.* **2009**, *395*, 156–161. [[CrossRef](#)]
38. Tsybenko, H.; Tian, C.; Rau, J.; Breitbach, B.; Schreiber, P.; Greiner, C.; Dehm, G.; Brinckmann, S. Deformation and phase transformation in polycrystalline cementite (Fe<sub>3</sub>C) during single- and multi-pass sliding wear. *Acta Mater.* **2022**, *227*, 117694. [[CrossRef](#)]
39. Chen, S.; Aitken, Z.H.; Pattamatta, S.; Wu, Z.; Yu, Z.G.; Srolovitz, D.J.; Liaw, P.K.; Zhang, Y.-W. Simultaneously enhancing the ultimate strength and ductility of high-entropy alloys via short-range ordering. *Nat. Commun.* **2021**, *12*, 4953. [[CrossRef](#)]
40. Ali, N.; Li, J.; Zhang, L.; Zhang, C.; Zhou, H.; Liu, D.; Sanaullah, K.; Nian, Y.; Cheng, J. Break the strength and ductility trade-off in novel NbC reinforced Fe<sub>40.5</sub>(CoCr)<sub>25</sub>Mn<sub>17.5</sub>Ni<sub>10</sub>Si<sub>5</sub> high entropy alloy. *Mater. Design.* **2024**, *239*, 112752. [[CrossRef](#)]
41. Zhou, H.W.; Bai, F.M.; Yang, L.; Wei, H.L.; Chen, Y.; Peng, G.S.; He, Y.Z. Mechanism of dynamic strain aging in a niobium-stabilized austenitic stainless steel. *Metall. Mater. Trans. A* **2018**, *49*, 1202–1210. [[CrossRef](#)]
42. Zhou, H.W.; He, Y.Z.; Cui, M.; Cen, Y.W.; Jiang, J.Q. Dependence of dynamic strain ageing on strain amplitudes during the low-cycle fatigue of TP347H austenitic stainless steel at 550 °C. *Int. J. Fatigue* **2013**, *56*, 1–7. [[CrossRef](#)]

**Disclaimer/Publisher’s Note:** The statements, opinions and data contained in all publications are solely those of the individual author(s) and contributor(s) and not of MDPI and/or the editor(s). MDPI and/or the editor(s) disclaim responsibility for any injury to people or property resulting from any ideas, methods, instructions or products referred to in the content.